Prediction of vascular injury by cavitation microbubbles in a focused ultrasound field

Yaqian Xie [a], Jiwen Hu [a,*], Weirui Lei [a], Shengyou Qian [b]

[a] College of Mathematics and Physics, University of South China, Hengyang 421001, China
[b] College of Physics and Electronics, Hunan Normal University, Changsha 410081, China

ARTICLE INFO

ABSTRACT

Many studies have shown that microbubble cavitation is one mechanism for vascular injury under ultrasonic excitation. Previous work has attributed vascular damage to vessel expansions and invaginations due to the expansion and contraction of microbubbles. However, the mechanisms of vascular damage are not fully understood. In this paper, we investigate, theoretically and experimentally, the vessel injury due to stress induced by ultrasound-induced cavitation (UIC). A bubble-fluid-vessel coupling model is constructed to investigate the interactions of the coupling system. The dynamics process of vessel damage due to UIC is theoretically simulated with a finite element method, and a focused ultrasound (FU) setup is carried out and used to assess the vessel damage. The results show that shear stress contributes to vessel injury by cell detachment while normal stress mainly causes distention injury. Similar changes in cell detachment in a vessel over time can be observed with the experimental setup. The severity of vascular injury is correlated to acoustic parameters, bubble-wall distance, and microbubble sizes, and the duration of insonation..

1. Introduction

Cavitation and bubble dynamics near solid boundaries have been investigated both theoretically and experimentally in many fields. On one hand, cavitation damage is the progressive loss of material in equipment in hydraulic environments [1,2], such as pumps, water turbines, and propellers, significantly shortening the life of these systems. On the other hand, cavitation effects are being exploited for numerous applications in chemistry [3], in medicine [4,5], and in environmental protection [6]. Of course the bubble will do this regardless of whether it is near a boundary or not. More importantly, the bubble loses its spherical symmetry when it is near a boundary [7]. The shock wave and micro-jet during bubble collapse are viewed as the two main mechanisms for ultrasonic cavitation damage, and even crack on the material surface [7,8].

A microbubble collapsing near a tissue boundary generates intense shear stress, which affects the membrane integrity [9] and eventually causes cell detachment when subjected to sufficiently high shear stress by liquid jets [10]. A shear stress of 100–160 Pa may be required for the detachment of the cultured cells [11] while a shear stress around 800 Pa cause the lysis of endothelial cells [12]. Being inspired by UIC

destruction to soft compliant wall, Curtiss et al. suggested that UIC may provide an efficient method for removing unwanted material layers off an attached surface, such as removing cholesterol from the aortic artery [13] destroying normal collagen and an elastic fibrous skeleton from thrombi and atherosclerotic plaques [14,15]. Bubble cavitation by regulating acoustic parameters have potential applications in the delivery of intravascular drugs and genes to regions of pathology [16–18], opening the blood–brain barrier (BBB) locally [19] and so on. However, acoustic cavitation dynamics in non-invasive, focused ultrasound therapies, such as shock wave lithotripsy [20] and histotripsy [21], thrombolysis [22], is usually accompanied with vascular rupture by shear stress [20–22].

Microbubbles confined in blood vessel have complicated dynamic behaviour when excited by an ultrasound and create multiple effects, including a cavitation effect, acoustic radiation force, acoustic streaming and sonoporation effect [23]. These mechanisms may result in structural modification of vessel, such as occlusion [1] and destruction [2], promoting drug penetration through the vessel wall or cell membrane. In both simulations and experiments, characterization of the bubble-vessel dynamics has been difficult. Experimentally, the challenge lies in performing measurements and observations in tissues and blood vessels due

---

to fast temporal scales and small spatial. As a result, experiment tal investigation has primarily been performed in vitro, typically making use of gels and vessel phantoms to model tissues and blood vessels, respectively [7,24–26]. The first direct in vivo observation of microbubble dynamics inducing microvessel ruptures were reported by Caskey et al. [27]. In that study, microbubble expansion constrained inside small vessels was significantly reduced, and the cavitation bubbles collapse asymmetrically in the vicinity of vessel wall. Inspired by this Chen et al. [28,29] performed analogous experiments in ex vivo rat mesentery. They found three mechanisms may potentially lead to the mechanical damage of blood vessels due to cavitation bubble. These include vessel invagination due to bubble collapse, vessel distention due to bubble growth, and puncturing of the vessel wall due to bubble jetting. These biomechanical effects create unintended and unwanted permanent damage to the blood vessel. However, UIC force can be exploited for drug delivery if the ultrasound parameters are well optimized [23]. Interestingly, UIC is utilized for a promising method for atherosclerotic inducement in animal models [30,31]. In this case, Shi et al. employed an ultrasonic standing wave with the participation of cavitation nuclei and by modulating the positions of the antinodes to obtain the positions of vessel-wall cavitation injury and the degree of vessel endothelial injury [31]. Silvani et al. [32] found that the use of pre-existing bubbles can lowers the intensity of ultrasound irradiation thereby mitigating potential adverse bioeffects, e.g., apoptosis, necrosis, and bleeding, and provide an integrated platform for precise and repeatable in vitro measurements of cavitation-enhanced endothelium permeability. By combining ultrasound with microbubbles, Yemane et al. [33] investigate the influence of vascular parameters on extravasation and the penetration of microbubble into the extracellular matrix by intravital multiphoton microscopy. They also found microbubbles could infiltrate the blood vessel, and there was a correlation between blood vessel size where extravasation occurred and mechanical index during ultrasonic excitation.

Besides experimental reports, computational models, which cannot be easily with experiments and can provide more details and insights about cavitation physics, have been utilized to depict the dynamics of bubbles confined inside blood vessels. Sassaroli and Hynynen [34] illustrated the frequency responses generated by an oscillating microbubble inside a small blood vessel, and revealed how the resonance frequency of microbubbles is influenced by the vessel radius, bubble radius and bubble position in blood vessels. Qin and Ferrara [35] gave similar predictions using a finite element method and also predicted the radius of the bubble as a function of time. A numerical model from Miao and Gracewski [36], using a coupled finite element and boundary element method to model the bubble shape with time, predicted the maximum tube dilation and maximum hoop stress occurred before the bubble reached its maximum radius as a bubble centered within a deformable tube. The model also indicated that when the tube radius, tube thickness and acoustic frequency were reduced, the maximum hoop stress increased, suggesting a higher potential for tube hemorrhage and rupture. A theoretical model coupled to the Navier–Stokes equations was given by Martynov et al. [37] and was used to demonstrate the wall deformations induced by an oscillating bubble within an elastic blood vessel. To find out what the cause of blood–brain barrier (BBB) disruption, Wiedemair et al. [38] developed a coupled multi-domain model through incorporation of the vessel structural dynamics, bubble dynamics and their interactions with the luminal liquid. They concluded that transmural pressure and wall shear stress at the luminal endothelial interface were two prominent factors for improving the efficiency of drug delivery. Based on the model presented by Wiedemair, Hosseinkhah et al. [24] created a finite element model combined with bubble-fluid-vessel system, and confirmed that vascular damage could occur during vascular invaginations due to the microbubbles' shrinkage. A similar model has also been treated by Chen et al. [39] and was used to demonstrate the influences of both acoustic parameters and material properties, including vessel size, microbubble shell visco-elastic

parameters and fluid viscosity, on the dynamic interactions in the bubble–blood–vessel system. A numerical model from Singh et al. [40], using combined laser and ultrasound to generate enhanced cavitation activity inside blood vessels, was carried out with finite element method. The results from this model indicated the laser play a significant role for small bubbles with radius less than 100 nm. Based on their previous work, Singh and Yang [41] created a 3D finite element method model for investigating the tangential or circumferential stress of the vessel wall. The simulation results showed shear stress generated by oscillating bubble was related to the bubble-vessel wall distance, and the bubble moved closer to the vessel wall over time. Interestingly, based on UIC force, Rigatelli et al. [42] created a computational model for assessing the potential of UIC damage to coronary artery endothelium and to promote atherosclerotic plaque progression.

As reported above, wall stress in vessels is critical in the cell distortion, and can mediate cellular functions or even damage the cytoskeletal structure if excessively large [43]. However, the majority of previous studies tend to report the vascular damage induced by the vessel expansion and invagination during bubble expansion and collapse, or evaluate the effect of vessel wall stresses on non-invasive BBB opening and UIC sonoporation to realize spatiotemporal-controllable drug delivery in selected regions using focused ultrasound. Many aspects of the mechanical mechanisms involved in the cavitation injury by stresses in action in cell detachment from vessel walls have remained obscure. In this paper, we focus on the mechanism of vascular injury, especially the dynamic behavior of cell detachment by UIC shear stress. A two-dimensional (2D) finite element method model is presented to simulate microbubble-cell interaction. The efficiency of cell detachment is presented for evaluating the vessel damage. To further assess the shear stress injury to the vessel wall, an ex vivo vascular model is tested with the designed FU setup, and discussions are made by comparing the current experimental observations with the theoretical simulation results.

2. Theoretical model and methods

2.1. Bubble-fluid-vessel model

A 2D geometry of the bubble–blood–vessel system is shown schematically in Fig. 1, where the microbubble is located close to one side of the vessel walls, L is the length of the vessel, d is the thickness of the vessel wall, R_v is the initial radius of the vessel, R_d is the distance between the initial bubble center and the vessel wall. The origin of the rectangular coordinate system (i.e. xy-coordinate plane) is at the lower-vessel center, the y coordinate is orthogonal to the vessel wall and the x coordinate is parallel to the vessel wall.

Assuming that gas inside the bubble is assumed spatially uniform and satisfies the ideal gas equation, the gas pressure inside the bubble changes with the bubble radius,

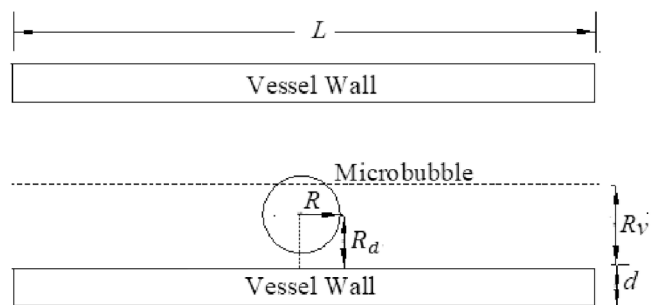$$p_g = p_{g0}\left(\frac{R_0}{R}\right)^{3\gamma} \tag{1}$$

Fig. 1. A schematic diagram of a bubble–blood–vessel system.

Where p_g is the gas pressure inside the bubble, γ is the polytropic exponent of the gas, R_0 is the initial radius of the bubble and R is its radius at time t. p_{g0} is the initial pressure and meets the static balance condition [44],

$$p_{g0} = p_0 + \frac{2\sigma'}{R_0} \tag{2}$$

Where σ' is the surface tension. When the length of the vessel is much greater than the bubble size, the fluid at both ends of the vessel will satisfy the boundary condition of $p_\infty = p_0 - p(t)$, where p_0 is the hydrostatic pressure in the fluid and $p(t)$ is the driving ultrasonic pressure pulse. For a gas bubbles oscillating in a incompressible fluid, the gas--fluid interface must obey a velocity continuity condition and a pressure continuity condition, which is given respectively as follows [39].

$$u(R) = \dot{R} \tag{3}$$

$$p(R) = p_g - \frac{2\sigma_g}{R} - 4\mu \frac{\dot{R}}{R} \tag{4}$$

Here σ_g is the interfacial tension of the free gas bubble.

Blood in the vessel is assumed as a homogeneous, incompressible and single-phase Newtonian fluid. If a bubble is excited by ultrasound, the fluid around the bubble must obey the mass and momentum conservation laws [24]:

$$\frac{\partial \rho}{\partial t} + \nabla \cdot (\rho \overrightarrow{u}) = 0 \tag{5}$$

$$\rho \left(\frac{\partial \overrightarrow{u}}{\partial t} + (\overrightarrow{u} \cdot \nabla) \overrightarrow{u} \right) + \nabla \cdot \left(-p \overrightarrow{I} + \mu_f \left(\nabla \overrightarrow{u} + \nabla \overrightarrow{u}^T \right) \right) = 0 \tag{6}$$

where $\overrightarrow{u}$ and $\overrightarrow{I}$ are the velocity vector and identity tensor, p is the pressure in the fluid, ρ and μ_f are the density and dynamic viscosity of the blood, respectively.

The vessel wall is assumed to be a homogeneous isotropic linear elastic material, which satisfy the displacement equations:

$$\rho_S \frac{\partial^2 \overrightarrow{d}_S}{\partial t^2} - \nabla \cdot \overrightarrow{\sigma} = 0 \tag{7}$$

Where ρ_S is the vessel density, $\overrightarrow{\sigma}$ is the stress tensor, which satisfies isotropic linear elastic constitutive equation [45]:

$$\overrightarrow{\sigma} = \lambda \, Tr(\overrightarrow{\varepsilon}) \, \mathbf{1} + 2\mu \overrightarrow{\varepsilon} \tag{8}$$

Where λ and μ are scalar constants known as Lamé coefficients, which are related to the elastic modulus E and the Poisson ratio ν, that is, $\lambda = \nu E/(1+\nu)(1-2\nu)$ and $\mu = E/2(1+\nu)$. The strain tensor $\overrightarrow{\varepsilon}$ satisfies the following equation [45]:

$$\overrightarrow{\varepsilon} = \nabla^S \, \overrightarrow{d_S} = \frac{1}{2} \left(\overrightarrow{d_S} \; \otimes \; \nabla + \nabla \; \otimes \overrightarrow{d_S} \right) \tag{9}$$

On the fluid-vessel interface, the stresses of the vessel wall are given as.

$$\sigma_n = \left(-p \overrightarrow{I} + \mu_f \left(\nabla \overrightarrow{u} + (\nabla \overrightarrow{u})^T \right) \right) \cdot \overrightarrow{n} \tag{10}$$

and

$$\sigma_\tau = \left(-p \overrightarrow{I} + \mu_f \left(\nabla \overrightarrow{u} + (\nabla \overrightarrow{u})^T \right) \right) \cdot \overrightarrow{\tau} \tag{11}$$

Where $\overrightarrow{n}$ and $\overrightarrow{\tau}$ are the unit vectors in the normal and tangential directions at the fluid–vessel interface. In addition, the fluid-vessel interface must also satisfy the conditions of velocity continuity and pressure continuity:

$$\overrightarrow{u}_f = \frac{\partial \overrightarrow{d_S}}{\partial t} \tag{12}$$

$$\overrightarrow{\sigma}_f \cdot \overrightarrow{n}_f = \overrightarrow{\sigma}_s \cdot \overrightarrow{n}_s \tag{13}$$

Where $\overrightarrow{u}_f$ is the fluid velocity vector, $\overrightarrow{d_S}$ is the wall displacement vector, $\overrightarrow{\sigma}_f$ and $\overrightarrow{\sigma}_s$ are the stress tensors of the fluid and vessel, respectively.

The degree of cavitation damage within the vessel is determined by the stresses exerted on the cell. When the forces exerted are sufficient, cell–cell breakage may occurs and leads to wall rupture.

2.2. A dynamic model of cell detachment efficiency

The dynamics of cell detachment from vessel wall under shear stress is a complicated process. We assume that i)cells are uniformly distributed within the vessel wall, ii) bubble–bubble interactions are ignored because of low bubble concentration, and iii) blood vessel injury is positively relate to cell detachment efficiency.

The kinetics may be expressed by a linear relationship. In this way, the number of detached cells as a function of time t and shear stress $\sigma_\tau N(\sigma_\tau, t)$ verifies [46].

$$\frac{dN(\sigma_\tau, t)}{dt} = -k(\sigma_\tau) N(\sigma_\tau, t) \tag{14}$$

Equation (14) suggests that cells detach independently, and the detachment probability per unit time is independent of time when taking no possible physical causes of fatigue during the cell-detachment process. Solving Eq. (2) leads to [46].

$$N(\sigma_\tau, t) = n(\sigma_\tau)(1 - e^{-k(\sigma_\tau)t}) \tag{15}$$

Where the values of both the detachment efficiency $n(\sigma_\tau)$ at infinite time and the detachment rate $k(\sigma_\tau)$ are determined by the applied shear stress, which is given as [47].

$$k(\sigma_\tau) = k_0 \frac{\exp(\sqrt{\sigma_\tau/4\sigma_{\tau 0}})}{(\sigma_\tau/4\sigma_{\tau 0})^{1/4}} \tag{16}$$

Where k_0 and $\sigma_{\tau 0}$ are two constants, which were determined experimentally by Décavé [48]. In the simulations, we applied these constants for bonding strength of vessel cells and used the parameters $k_0 = 2 \times 10^{-4}$/s and $\sigma_{\tau 0} = 8 \times 10^{-2}$ Pa [48].

Another hypothesis considers that detachment will not occur below a threshold stress σ_τ for a given cell on a given surface. If $f(\sigma_\tau)$ is the distribution function of threshold stress in the cell population, $n(\sigma_\tau)$ is given by Zakerzadeh and Zunino [46].

$$n(\sigma_\tau) = \int_0^{\sigma_\tau} f(\sigma_\tau) d\sigma_\tau \tag{17}$$

An approximate expression of $f(\sigma_\tau)$ is obtained assuming a log-normal distribution σ_τ [46].

$$f(\sigma_\tau) = \frac{1}{\overline{\sigma}\sqrt{2\pi}} \exp\left(-\frac{[\ln(\sigma_\tau) - \ln(\overline{\sigma})]^2}{2\overline{\sigma}^2}\right) \tag{18}$$

Where parameter $\overline{\sigma}$ is the nondimensional variance, and is $0.60 \sim 0.62$ in our calculations.

2.3. A dynamic model of vessel damage

Blood vessel damage is defined as the irreversible rupture of the cell–cell network and process of the cell detachment. It consists of a cumulative damage due to low strength for long-duration loads and one time-loss injury subjected to relatively high strength or fast loading. A theoretical description of the vessel damage is fairly complicated, which is not only correlated with the characteristics of the biological tissue

itself, such as stress relaxation, and hysteresis, both of which are dependent on the timescales of deformation, but also to related to the external stress, for instance, the stress/strain histories caused by different loading sequences.

It is assumed that vessel injury will takes place if the external pullout force exceeds the breaking strength of cell–cell detachment as given in Eqs. (14)-(17). To account for the breaking of cell–cell bonds perhaps some modification could be made to the vessel damage when subjected to a time-varying stress. The general form of the rate of damage function, which expresses the damage accumulation due to stress, may be written as follows:

$$\dot{D}(t) = \psi(E_D, \sigma(t)) \tag{19}$$

In Eq. (19), $D(t)$ dot denotes differentiation with respect to time t, E_D is an damage energy for irreversible damage reaction and is a constant.

We assume that the vessel wall is homogeneous and isotropic, the strain energy density function, w, may be written as:

$$w(\sigma) = \frac{1}{2}\left(\frac{\sigma_\tau^2}{\kappa_G} + \frac{\sigma_n^2}{\kappa_E}\right) \tag{20}$$

Here parameters κ_G and κ_E are shear modulus and Young's modulus of tissue, respectively.

Based on an Arrhenius integral model for thermal cumulative damage of soft tissues [49], a combined energy–stress prediction model combined with Eqs. (19) and (20) is assumed to depend upon the instantaneous stress level and the previous stress history, and is estimated by the tissue damage rate $D(t)$ expressed in the form:

$$D(t) = \int_0^{t_F} \exp\left(-\frac{A\,E_D}{\sigma^2(t)}\right) dt \tag{21}$$

Here, symbol t_F denotes sonication time, parameter A is the material parameter, associated with vessel elasticity containing material properties of Young's modulus and shear modulus. Parameters A and E_D are assumed to be 1.0×10^9 N and 1.0×10^5 J per unit volume [49], respectively. We also assume that D has a value of zero initially, when the cell vibrates in the overload state, and increases monotonically, reflecting the cell's exposure to time-varying stress. The rupture or detachment of a particular cell from vessel wall is indicated when the cell reaches a critical value of the damage-energy index E_D.

2.4. Numerical simulation

Based on the model as illustrated in the schematic diagram of Fig. 1, the vessel damage is studied due to interactions of cavitation microbubble and vessel wall in a FU field, where the FU focus is set to be located in the middle of vessel lumen. The vessel length in the whole study is L = 200 μm. According to the distribution characteristics of the stress force, the relative microbubble scale can be viewed as infinite. The simulation parameters are listed in Table 1. Equations of bubble-fluid-wall interaction with initial and boundary conditions are solved by a method based on finite element method via COMSOL Multiphysics 5.0

(Comsol, Inc.; Burlington, MA). In the model as depicted in Fig. 1, unit size free triangle mesh is applied to partition the model. A maximum mesh size of λ/6 (λ is the acoustic wavelength) in the focal region and a maximum mesh size of λ/4 in the rest of the domain is utilized to generate grid. The vessel walls contain 5086 vertices of mesh and 9570 triangular elements. In addition, the blood is consisted of 9570 triangular units and 4937 vertices.

3. Results and discussion

3.1. Simulation results

To investigate the detachment kinetics of cells a set of detachment curves is obtained by using Eq. (15). Fig. 2 shows time variation of the percentage of detached cells (PDC) rises over time and reaches a plateau at three different shear stresses σ_τ = 100, 150, and 300 Pa. The characteristic time to reach the plateau is shorter at higher stresses. It is seen that at any σ_τ the shear stress increases with time and eventually attains a steady state. The level of the plateau is higher for higher stresses. The kinetics obeys a first-order relationship. The number of detached cells verifies that cells detach independently.

Fig. 3 depicts the PDC distributions as a function of position along the vessel wall during FU exposures with a 4-cycle, 1.18 MHz continuous sine wave, and a negative pressure of around 4.3 MPa at the FU focus. As is expected, the cell disruption is instantaneous according to Eq. (15). Fig. 3 clearly shows a very rapid and large initial loss of the cell detachment generated by an oscillating bubble with an initial radius of $R_0 = 2.5$μm in a very short period of time. After the 4-cycle shear stress exposure, PDC increases from 0.43 in one cycle to 0.82 in four-cycle times. Such results are qualitatively consistent with some reports on cell damage [51,52]. The kinetics of cell detachment is strongly affected by the applied shear stress and the substrate properties. Equation (17) indicated a log-normal distribution function of threshold shear. There are no reports about the shear stress thresholds to the endothelial cells on vessel walls. Therefore, an estimated threshold of 100 Pa is used in our simulations for computation according to the detachment of cultured HeLa cells by Ohl et al.[11]. The results indicate that endothelial cells would eventually detach when the shear stress exceeds a threshold [12], but the cell detachment gradually tends to a stable value.

To evaluate the vessel injury, we give a 2D wall morphology, based on equation (21), that demonstrates the damage evolution with time as shown in Fig. 4. Two characteristic phenomena have been observed
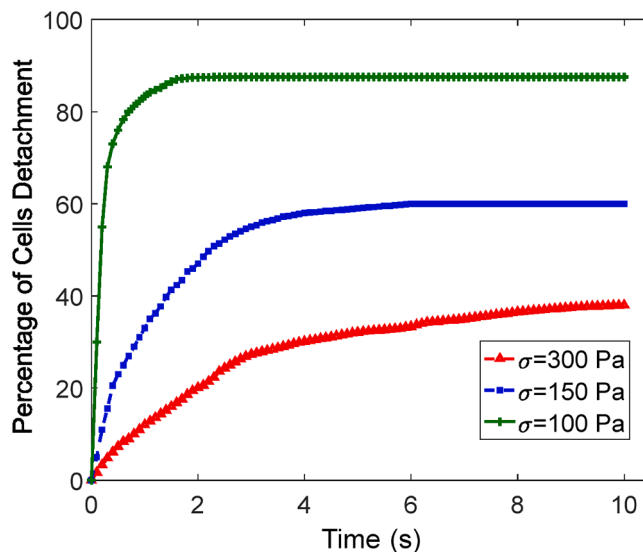
Table 1
Values of parameters in this study [50].

Name	parameter	Value(unit)
Gas polytropic	γ	1.17
Saturated vapor pressure	P_v	2330 Pa
The initial radius of the microbubble	R_0	2 μm
Gas-liquid surface tension	σ_g	0.056 N·m^{-1}
The density of blood	ρ	1059 kg·m^{-3}
Sound pressure	P_a	0.1–0.2 MPa
Hemodynamic viscosity	μ	0.0035 Pa·s
Blood vessel density	ρ_S	1000 kg·m^{-3}
Young's modulus of blood vessel	E	1.0 MPa
Vascular Poisson's ratio	ν	0.49

Fig. 2. Cell detachment efficiency at the indicated shear stress as a function of time.
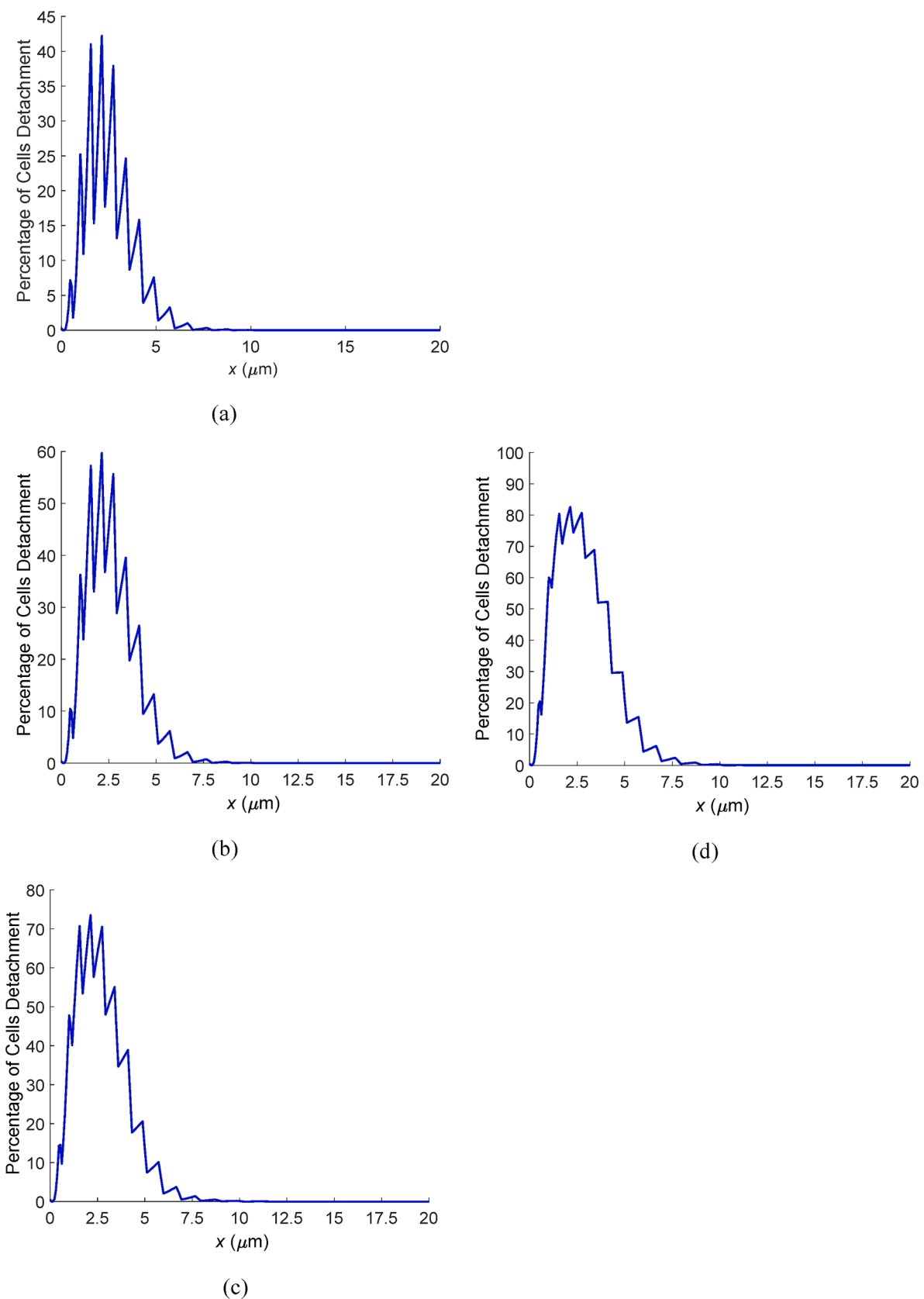
(a)

(b)

(d)

(c)

Fig. 3. Cell detachment efficiency as a function of position by a cavitation bubble insonified with a continuous sine wave for out power of 180 W during four successive cycles: (a) one cycle, (b) two cycles, (c) three cycles, and (d) four cycles.
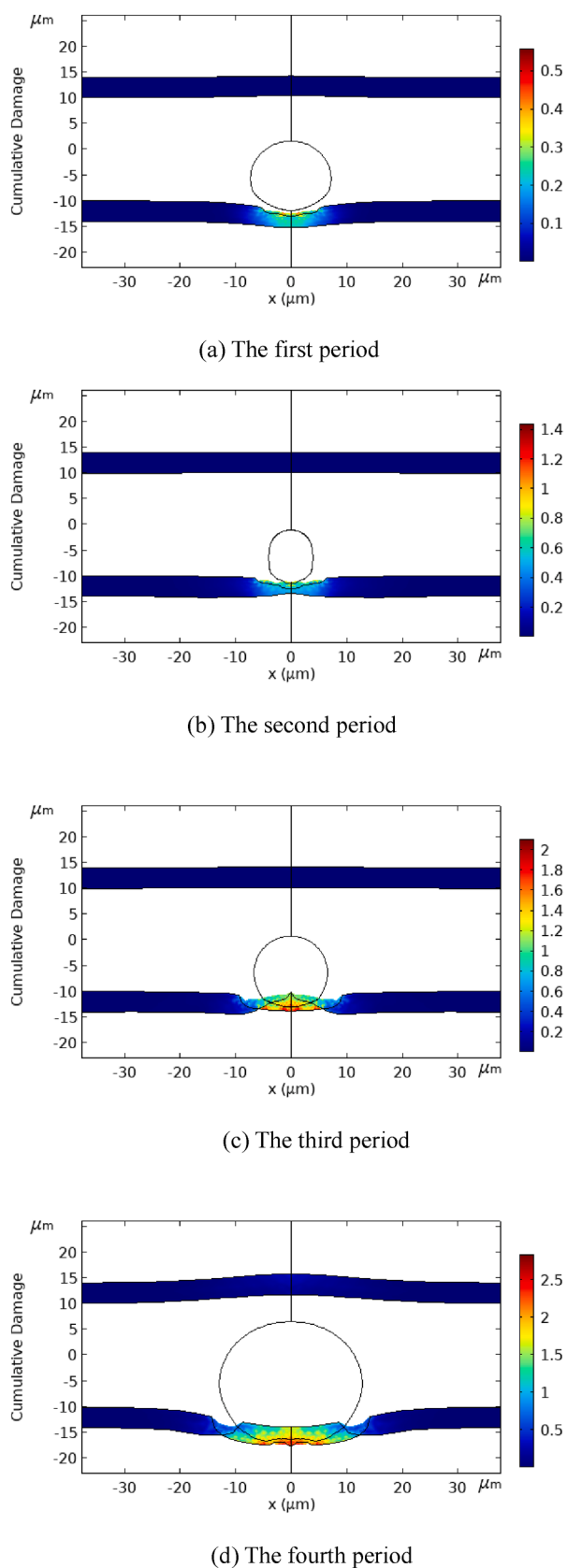
(a) The first period

(b) The second period

(c) The third period

(d) The fourth period

Fig. 4. Damage evolution profiles at different periods.

from the figure: on the one hand, the cavitation bubble oscillates with a non-spherical shape and shows a migration towards the vessel boundary. On the other hand, vessel injury occurs at surface in the first period and becomes more severe with insonation time. Note that the temperature elevation in vessel tissue can be neglected for a short duration of ultrasonic radiation. In addition, the stress profile induced by microjet on the vessel wall is not depicted in this figure, which has been investigated in our previous work [53]. Making careful observations of vessel shape and damage color changes in the bubble–blood–vessel interactions, one found in Fig. 4(a)–(c) that cell detachment by shear stress is the main injury and accumulates over time when the vessel radius is far greater than the maximum size of a vibrating microbubble. While in some cases bubbles expanded to much larger sizes compared to bubble sizes, vessel distention may play a more important role than shear stress in causing vessel injury, especially at the outer vessel wall as illustrated in Fig. 4(c) and (d). Some experiments have suggested that vascular injury from acoustically activated bubbles has been attributed to either high shear stress by liquid jet [54] or vessel distention due to "pushing" forces [28,29,55].

Fig. 5 demonstrates the correlation between percentage of cell detachment at various distances R_d for a bubble with an initial radius of 2.5 μm, an acoustic driving pressure of 0.2 MPa, and a driving frequency of 1.18 MHz. It can be seen that the damage gradually decreases with cavitation bubble staying away from vessel wall. The maximum detachment decreased from 48 % for $R_d = 6.0$ μm down to 39 % for $R_d = 9$ μm.

In addition, we also found that the cell detachment was related to the initial radius R_0 for a frequency. As shown in Fig. 6, the percentage of cell detachment decreased with increasing R_0 for three frequencies (i.e. 1 MHz, 2 MHz and 3 MHz), and decreases more quickly in higher frequency with increasing initial radius R_0, which was consistent with the trend in the results reported by Qin and Ferrara [35]. Noted is that, for the frequency of 1 MHz and the vessel radius of 5 μm, the cell detachment in one minute reached a peak value when bubble with initial radius is 1.5 μm and then drops with increasing R_0. The results suggest that the cavitation damage in blood vessels must be combined with the vessel size, initial bubble radius and driving frequency.

3.2. Experimental method and results

3.2.1. Experimental setup

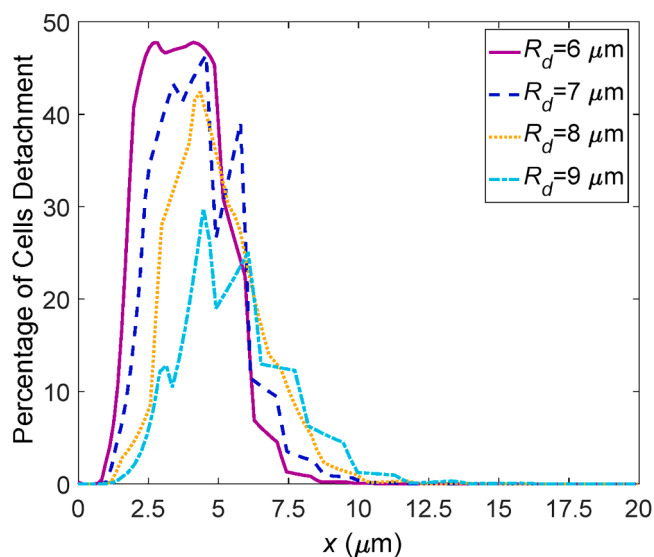Ex vivo vascular model is tested with the designed focused

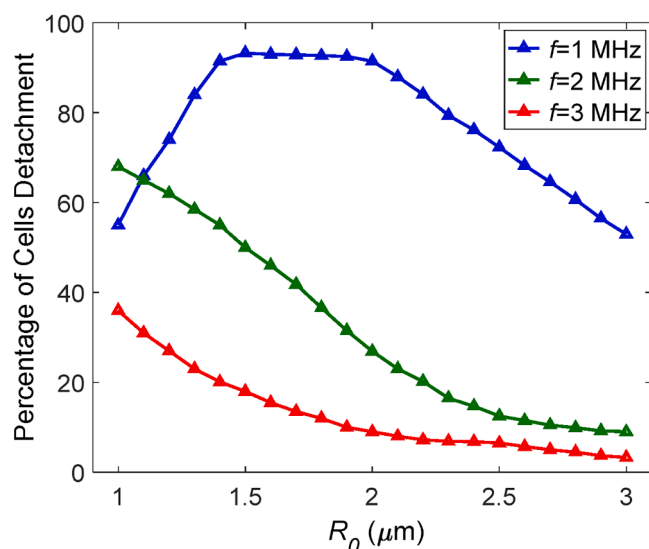**Fig. 5.** Percentage of cell detachment at the first period for four different distances.

Fig. 6. The percentage of cell detachment at different initial radius.

ultrasound (FU) system (PRO2008, Shenzhen PRO-HIFU Medical Tech. Co., ltd, China) to evaluate the degree of cell detachment by UIC during FU exposure. Fig. 7(a) illustrates the experimental setup for the ex vivo FU radiation. The main parameters of the setup are as follows: 1.18 MHz, focal lengths 13 cm. The sound intensity is $2 \sim 10$ kW/cm^2, a general power of 120–280 W. Ultrasound radiation with peak negative pressures (PNP) of 3.5–6.5 MPa is used in this setup.

An ultrasound imaging device (EnVisor, Philips, Holland) is used for monitoring of the cavitation activity by hyperechoic area induced by cavitation bubbles within the artery model. This imaging probe (4–6 MHz) is incorporated into the center of the FU transducer head. The vascular geometric model is acquired from broiler chicken intestinal, and is packaged for six groups. The initial inner radius, outer radius, and length of each specimen are respectively 5.1 mm, 6.5 mm, and 70 mm, which is relatively close to the size of the arteries.

3.2.2. Experimental method

The vascular models are stored in the refrigerator at temperature of 0 °C prior to testing, and then are placed at a constant external temperature of 37 °C for about an hour. To reduce injuries caused by shock wave as much as possible, vascular model is firmly fixed in a small slot of absorbing tile, which is positioned at the beam focus. To achieve a high probability of cavitation bubbles within the vascular sample, the fluid inside and outside the sample is respectively filled with normal distilled water and degassed water, which is slowly flowing down the inner wall of the glass tank with a plastic pipe according to the principle of siphoning until the bottom of the FU probe is submerged above 10 cm. In addition, the absorbing tiles are sticked to the bottom of the water tank to get rid of the reflected ultrasound wave as shown in Fig. 7(b).

Function waveform generators produces continuous wave signal to drive FU transducer. Two out power are chosen: 120 W and 180 W.
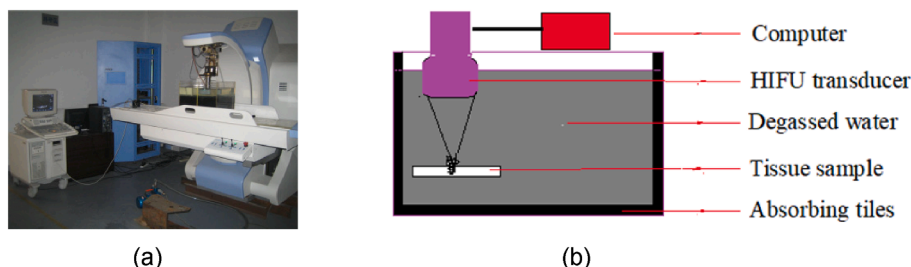
Ultrasound imaging system record the cavitation phenomena at each power level simultaneously. The artery model samples are sonicated for 2–3 min. The results and damage of the samples after continuous wave exposures are examined by light microscope (L135A, 10*100X) for all output power levels.

3.2.3. Experimental results

After FU radiation, each sample is cut in the longitudinal direction. Fig. 8 shows the evolution of cell detachment profiles at three times $t = 1$ s, 30 s, and 60 s. Tube wall become damaged and wider in the vicinity of the focal area with FU exposures. A non-homogeneous distribution of cell detachment in the wall at different time can be observed. In addition, unlike real-time response in the simulations as seen in Fig. 2, experimental results show there is a time–lagged effect between the cell detachment and shear stress as shown in Fig. 8(a). One possible explanation for this difference between numerical and experimental results is that fatigue effects may play a role in continually stress force before the cell detachment from endothelium. Another possible mechanism is that the cell–cell interaction may induce the resistance force against detachment force due to the spatial inhomogeneity distribution of the cytoskeletal structure [56].

It is noted that, in an experimental run, cell detachment generates not just a single bubble but a large cluster of bubbles. Furthermore, as can be observed in Fig. 8, it take one minute to cause all of the severe damage to the wall, while no damage, even for a comparatively high shear stress of about $800 - 1000$ Pa in FU focus can be found for the same FU radiation at the first one second as depicted in Fig. 8(a). The presence of the damage accumulation may be explained by a consequence of fatigue effects on continually stressed cells. Thus, cell damage by shear stress should be a function of time of exposure as well as shear stress [56].

The spatial extent of detachment in the tested sample tissue is obtained with statistical analysis, and the wall damage is evaluated by measuring the cell detachment area. The detached cells on vessel wall, expressed as a percentage occurrence in a histogram based on a mass-weighted method is shown in Fig. 9. At 1 s, 1.2 % of cells are observed to detach from the wall, where cell detachment is scarcely observed. At 10 s, 12 % of cells became detached, while 38 %, 90 % and 100 % are observed when the FU exposure times were 30, 60, and 72 s, respectively. It should be noted the ratio of detached cells to total cells is determined by penetrating the wall when the exposure time is 72 s. In addition, the PCD response in Fig. 9 exhibits a great similarity to the curve changes in Fig. 2 with time.

3.3. Discussion

In this study, a fully coupled bubble-fluid-vessel model is developed. The vessel injury due to stress induced by ultrasound induced cavitation are investigated theoretically and experimentally. In our computational model, an off-center bubble can be located at any position with a distance d near an elastic wall. Based on theory and experiment, two different damage models are used for evaluating the cumulative damage of blood vessels.
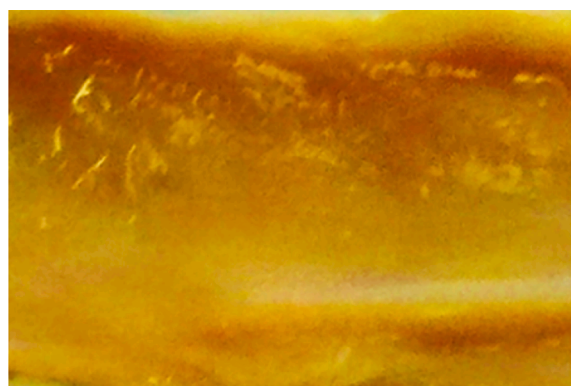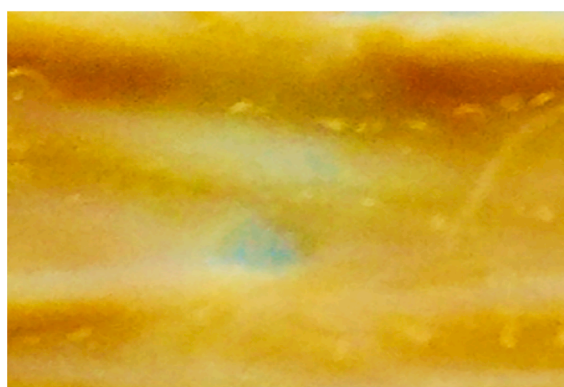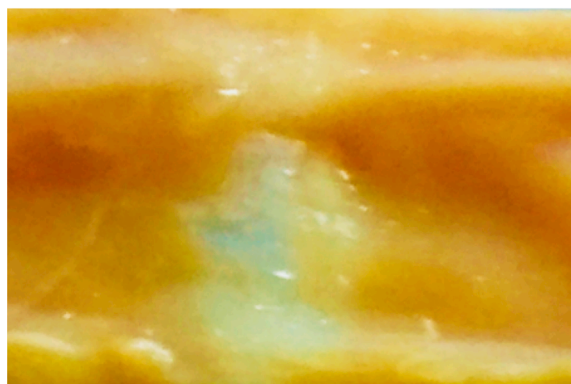

(a)   (b)

Fig. 7. Schematic of the experimental set-up: (a) physical drawing of FU system and (b) diagram of FU system.

(a) $t = 1$ s

(b) $t = 30$ s

(c) $t = 60$ s

Fig. 8. Evolution of cell detachment profile generated by FU radiation out power of 180 W at three times: (a) $t = 1$ s, (b) $t = 30$ s, and (c) $t = 60$ s.

Fig. 9. Percentage of cell detachment at different times for out power of 180 W.

Fig. 10. Comparison of vessel damage degree for out power of 180 W during four successive cycles: –■– represents the cumulative damage by cell detachment rate, and four data is extracted from the peak values in Fig. 3, –▼– represents the cumulative damage rate D and four data is extracted from the peak values in Fig. 4, an –◆– represents the square root of cumulative damage rate D.

The current numerical model is validated by simulation of vessel damage degree for solving Eqs. (15) and (21) combined with the analytical method and the finite element method. As shown in Fig. 10, the blue square–plotted curve (case I) represents the damage directly due to shear stress by solving Eq. (15) while the black triangle–plotted curve (case III) represent the damage due to strain energy disturbance by solving Eq. (21), and the red rhombus–plotted curve (case II) comes from the square root of case III. It can be seen clearly that the damage degree for three cases increases with the FU exposure time. Compared to case I and case II, the damage for case III, including the total work done by the tangential and normal stresses, produces a more serious injury to the vessel walls. Case I and case II have a similar trend and are becoming
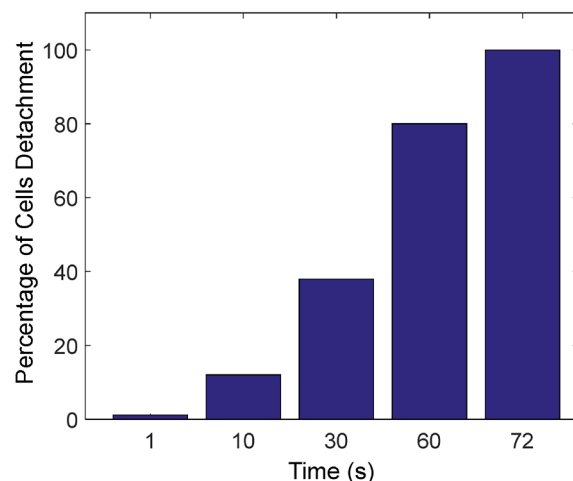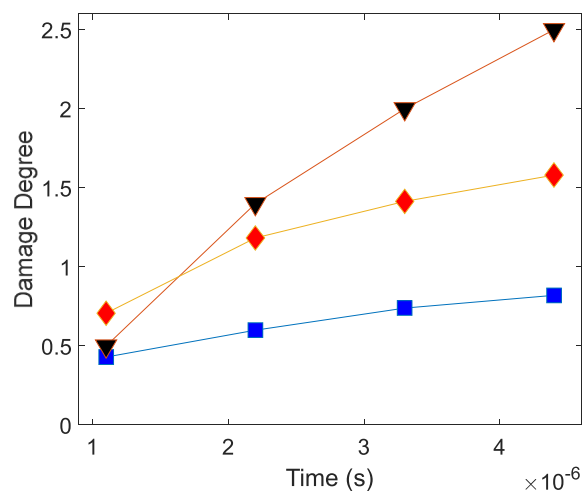
increasingly differentiated. It indicates case II has relatively great impact on vessel damage than case I with time. In fact, one can find, considering the relation between Eqs. (20) and (21), case II is the sum damage generated by tangential and normal stresses It may be inferred from the results of Fig. 10, for comparing Fig. 3 and Fig. 4, the difference between case I and case II may be the damage produced from normal stress. To this view, one can reasonably conclude that the rapid expansion and contraction of a oscillating microbubble, which has size comparable to that of the vessel radius, result in vascular injury or rupture due to the large normal stress as shown in Fig. 4(c) and (d), exhibiting excellent agreement with the experimental results reported by Chen [28,29]. In addition, as depicted in Fig. 4(a) and (b), when the vibration amplitude of bubbles is much smaller than vessel radius, vessel injury mainly depended on shear stress due to cavitation-induced microjet [24].

In the experiments section, we have primarily focused on cumulative effects of blood vessel induced by shear stress because the testing condition is based on the large blood vessels compared to microbubble. The damage evolution of vessel samples through experimental test has the similar tendency as displayed in Figs. 8 and 11. In regard to the size and
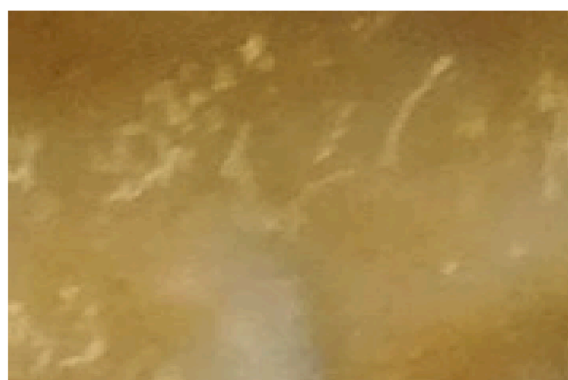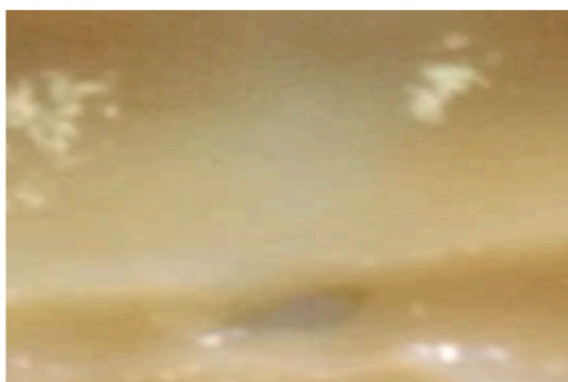
(a) $t = 1$ s

(b) $t = 30$ s

(c) $t = 60$ s

Fig. 11. Evolution of cell detachment profile generated by FU radiation at three times: (a) $t = 1$ s, (b) $t = 30$ s, and (c) $t = 60$ s.

shape of vessel injury both figures have some difference by comparing profile of Fig. 4. However, cavitation pits formed through experiments displays very similar types of the simulating results as shown in Fig. 4. Perhaps the fact that theoretical results are predictions based on single-bubble cavitation model while experimental testing of vessel injury for the collective effects of multiple microbubbles. If FU out power is reduced from 180 W to 120 W, as seen in Fig. 11, the vessel injury due to cavitation bubble in ultrasound field seem mild compared to that of in Fig. 8 for out power of 180 W. But both of them demonstrate the similar injury profiles in three different periods. Interestingly, when the blood sample is located at 14 cm (FU focus length 13 cm), it could be found that the distribution of cavitation damage is obviously difference. The

vessel damage of off-focus test was significantly reduced in comparison to the case of a FU focal point at the vessel center for the same time and out power, but the vessel injury area in Fig. 12 is actually significantly larger than those of Figs. 8 and 11. Besides, Fig. 12 has no obvious cavitation pits. These differences may be partly explained by the occurrence conditions of acoustic cavitation. The formation, growth and collapse of gas bubbles or vapor are closely related to the space-dependent acoustic field [57]. It is well known that cavitation bubbles usually start in the focal region where the acoustic pressure is the highest in the whole ultrasound field [58], but the acoustic pressure as well as the cavitation intensity decreases with off-focus distance. However, there is still a relatively large area for the blood vessel in the off-

(a) $t = 1$ s

(b) $t = 30$ s

(c) $t = 60$ s

Fig. 12. Evolution of cell detachment profile generated in off-focus region at three times: (a) $t = 1$ s, (b) $t = 30$ s, and (c) $t = 60$ s.

focus regions, where the pressure peak exceeds the cavitation threshold.

The results in Figs. 8, 11, and 12 suggest that acoustic output power relates to damage severity. The detachment efficiency as shown in Fig. 13 exhibits the PCD curve of vessel samples with changing output power, using the preceding experimental setup. The detachment efficiency increases rapidly with increasing out power, and, above 210 W, more than 90 % of the cells have been detached from vessel surface.

In conclusion, comparison between experimental and simulational results clearly shows that the injury area of vessel surface increases and the degree of vessel injury gradually intensified with FU irradiation. This can be confirmed by the morphology of two-dimensional vessel damage in Figs. 4, 8, 11and 12, which demonstrates the similar changing trend. The cumulative process of vessel damage is an irreversible under continuous stress applications or energy disturbance. The calculated results are in agreement with the experimental results.

It should be pointed that uncertainties and errors may exist in our work by the approximations and assumptions. First, a 2-D simplified model is simulated instead of a 3-D model to reduce the computing time, as a results direct observation of vessel surface injury can fail because of model simplification. Meanwhile, the assumptions of the model exclude many complicated but physically realistic situations, e.g., multi-bubble interactions, static Newtonian viscous fluid [59]. Moreover, the damage expression of equation (21) is obtained by a simple analogy to the thermal damage model proposed by Pérez-Maqueda [49]. In addition, we have assumed the constitutive model in this study is a linear elastic isotropic material. In fact, biological tissues and extracellular matrices exhibit far more complex mechanical behaviours, that is, an anisotropic nonlinear viscoelastic-viscoplastic property [60], which may bring difficulty in predicting the occurrence of tissue damage. Meanwhile, soft tissues show an obvious time-lagging effect similar to thermal response subjected to short pulse laser or FU irradiation [61], due to the fact that the force response propagates almost with an infinite speed through such medium [62], which may reduce vessel injury. Finally, fatigue damage by repeated cyclic loading on soft fibrous tissues is also an important factor in evaluating the damage progression, which has not so far been addressed in fatigue model of soft tissues [63]. The limitations mentioned above lead to some error between numerical simulation and experimental observation. For example, vessel damage response using simulation is faster than that of experimental test. Despite the limitations of the present models, the simulated results and ex-vivo vessel experiments are adequate in providing a quantitative prediction of the vessel damage, and show significantly better consistency with relative work reported before. It suggests that the presented model in this paper may be applied to help explain different types of vascular damage by UIC.

4. Conclusion

In this paper, a 2D finite-element method model is developed to simulate the two-way coupling interactions in the bubble–blood–vessel system. The detachment of cells from the tube wall by stresses is studied theoretically and experimentally. The numerical results suggested that vessel distention induced by normal stress and cell detachment generated by shear stress contributes to vascular injury. The efficiency of cell detachment is associated with vessel and microbubble size, and acoustic driving frequency. The cell detachment occurs when the shear stress exceeds the threshold strength of the wall, and reaches a stable value after a rapid increase for high shear stress. But, unlike real-time response in the simulations, experimental results show there may be a time-–lagged effect between the cell detachment and shear stress because of the nonlinear elasticity of the tissue. Overall, both theoretical and experimental results indicate that the vessel damage is a cumulative process, and is related to many factors, such as acoustic parameters, bubble-wall distance, etc.
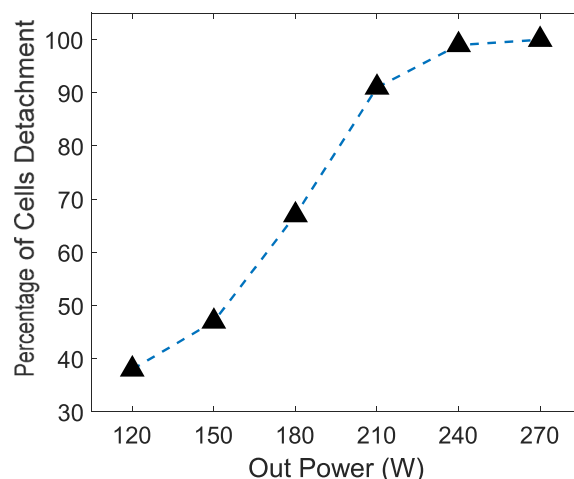

Fig. 13. Evolution of cell detachment profile generated for FU radiation time *t* = 30 s.

Declaration of Competing Interest

The authors declare that they have no known competing financial interests or personal relationships that could have appeared to influence the work reported in this paper.

Acknowledgments

References

[1] B. Ghiban, C.A. Safta, M. Ion, et al., Structural aspects of silt erosion resistant materials used in hydraulic machines manufacturing[J], Energy Procedia 112 (2017) 75–82, https://doi.org/10.1016/j.egypro.2017.03.1064.

[2] B.S. Thapa, O.G. Dahlhaug, B. Thapa, Sediment erosion in hydro turbines and its effect on the flow around guide vanes of Francis turbine[J], Renew. Sustain. Energy Rev. 49 (2015) 1100–1113, https://doi.org/10.1016/j.rser.2015.04.178.

[3] A. Barchouchi, S. Molina-Boisseau, N. Gondrexon, et al., Sonochemical activity in ultrasonic reactors under heterogeneous conditions[J], Ultrason. Sonochem. 72 (2021), 105407, https://doi.org/10.1016/j.ultsonch.2020.105407.

[4] Z. Izadifar, P. Babyn, D. Chapman, Ultrasound cavitation/microbubble detection and medical applications[J], J. Med. Biol. Eng. 39 (3) (2019) 259–276, https://doi.org/10.1007/s40846-018-0391-0.

[5] Šarc A, Kosel J, Stopar D, et al. Removal of bacteria Legionella pneumophila, Escherichia coli, and Bacillus subtilis by (super) cavitation[J]. 10.1016/j.ultsonch.2015.10.010.

[6] M. Dular, T. Griessler-Bulc, I. Gutierrez-Aguirre, et al., Use of hydrodynamic cavitation in (waste) water treatment[J], Ultrason. Sonochem. 29 (2016) 577–588, https://doi.org/10.1016/j.ultsonch.2015.10.010.

[7] L. Ye, X. Zhu, Analysis of the effect of impact of near-wall acoustic bubble collapse micro-jet on Al 1060[J], Ultrason. Sonochem. 36 (2017) 507–516, https://doi.org/10.1016/j.ultsonch.2016.12.030.

[8] K. Johansen, J.H. Song, K. Johnston, et al., Deconvolution of acoustically detected bubble-collapse shock waves[J], Ultrasonics 73 (2017) 144–153, https://doi.org/10.1016/j.ultras.2016.09.007.

[9] A. Priyadarshi, M. Khavari, T. Subroto, et al., On the governing fragmentation mechanism of primary intermetallics by induced cavitation[J], Ultrason. Sonochem. 70 (2021), 105260, https://doi.org/10.1016/j.ultsonch.2020.105260.

[10] S.R. Gonzalez-Avila, A.C. Van Blokland, Q. Zeng, et al., Jetting and shear stress enhancement from cavitation bubbles collapsing in a narrow gap[J], J. Fluid Mech. 884 (2020), https://doi.org/10.1017/jfm.2019.938.

[11] C.D. Ohl, B. Wolfrum, Detachment and sonoporation of adherent HeLa-cells by shock wave-induced cavitation[J], Biochimica et Biophysica Acta (BBA)-General Subjects 1624 (1–3) (2003) 131–138, https://doi.org/10.1016/j.bbagen.2003.10.005.

[12] M.W. Miller, Cell size relations for sonolysis[J], Ultrasound Med. Biol. 30 (10) (2004) 1263–1267, https://doi.org/10.1016/j.ultrasmedbio.2004.07.005.

[13] G.A. Curtiss, D.M. Leppinen, Q.X. Wang, et al., Ultrasonic cavitation near a tissue layer[J], J. Fluid Mech. 730 (2013) 245–272, https://doi.org/10.1017/jfm.2013.341.

[14] Porter T R, Xie F, Lof J, et al. The thrombolytic effect of diagnostic ultrasound induced microbubble cavitation in acute carotid thromboembolism[J]. Investigative radiology, 2017, 52(8): 477. 10.1097%2FRLI.0000000000000369.

[15] B. Zhang, H. Kim, H. Wu, et al., Sonothrombolysis with magnetic microbubbles under a rotational magnetic field, Ultrasonics 98 (2019) 62–71, https://doi.org/10.1016/j.ultras.2019.06.004.

[16] Z. Fan, R.E. Kumon, C.X. Deng, Mechanisms of microbubble-facilitated sonoporation for drug and gene delivery[J], Therapeutic delivery 5 (4) (2014) 467–486, https://doi.org/10.4155/tde.14.10.

[17] K. Kooiman, S. Roovers, S.A.G. Langeveld, et al., Ultrasound-responsive cavitation nuclei for therapy and drug delivery[J], Ultrasound Med. Biol. 46 (6) (2020) 1296–1325, https://doi.org/10.1016/j.ultrasmedbio.2020.01.002.

[18] Y.Y. Yang, Q.Y. Li, X.S. Guo, Xiasheng, Mechanisms underlying sonoporation: Interaction between microbubbles and cells, Ultrason. Sonochem. 67 (2020), 105096, https://doi.org/10.1016/j.ultsonch.2020.105096.

[19] C. Sierra, C. Acosta, C. Chen, et al., Lipid microbubbles as a vehicle for targeted drug delivery using focused ultrasound-induced blood–brain barrier opening[J], J. Cereb. Blood Flow Metab. 37 (4) (2017) 1236–1250, https://doi.org/10.1177/0271678X16652630.

[20] C. Hunter, A.D. Maxwell, B. Cunitz, et al. Impact of stone type on cavitation in burst wave lithotripsy[C]//Proceedings of Meetings on Acoustics 176ASA. Acoustical Society of America, 2018, 35(1): 020005. 10.1121/2.0000950.

[21] E. Vlaisavljevich, K.W. Lin, M.T. Warnez, et al., Effects of tissue stiffness, ultrasound frequency, and pressure on histotripsy-induced cavitation bubble behavior[J], Phys. Med. Biol. 60 (6) (2015) 2271, https://doi.org/10.1088/0031-9155/60/6/2271.

[22] S. Xu, Y. Zong, Y. Feng, et al., Dependence of pulsed focused ultrasound induced thrombolysis on duty cycle and cavitation bubble size distribution[J], Ultrason. Sonochem. 22 (2015) 160–166, https://doi.org/10.1016/j.ultsonch.2014.06.024.

[23] S. Lu, P. Zhao, Y. Deng, et al., Mechanistic Insights and Therapeutic Delivery through Micro/Nanobubble-Assisted Ultrasound[J], Pharmaceutics 14 (3) (2022) 480, https://doi.org/10.3390/pharmaceutics14030480.

[24] N. Hosseinkhah, H. Chen, T.J. Matula, et al., Mechanisms of microbubble–vessel interactions and induced stresses: a numerical study[J], J. Acoust. Soc. Am. 134 (3) (2013) 1875–1885, https://doi.org/10.1121/1.4817843.

[25] C.C. Church, X. Yang. A theoretical study of gas bubble dynamics in tissue[C]//AIP Conference Proceedings. American Institute of Physics, 2006, 838(1): 217-224. 10.1063/1.2210349.

[26] X.S. Guo, C.L. Cai, J.Y. Xu, et al., Interaction between cavitation microbubble and cell: A simulation of sonoporation using boundary element method (BEM), Ultrason. Sonochem. 39 (2017) 863–871, https://doi.org/10.1016/j.ultsonch.2017.06.016.

[27] C.F. Caskey, S.M. Stieger, S. Qin, et al., Direct observations of ultrasound microbubble contrast agent interaction with the microvessel wall[J], J. Acoust. Soc. Am. 122 (2) (2007) 1191–1200, https://doi.org/10.1121/1.2747204.

[28] H. Chen, A.A. Brayman, M.R. Bailey, et al., Blood vessel rupture by cavitation[J], Urol. Res. 38 (4) (2010) 321–332, https://doi.org/10.1007/s00240-010-0302-5.

[29] Chen Hong, Kreider Wayne, A. Brayman Andrew, R. Bailey Michael, J. Matula Thomas. Blood vessel deformations on microsecond time scales by ultrasonic cavitation.[J]. Phys. Rev. Lett. 2011,106(3). 10.1103/PhysRevLett.106.034301.

[30] Y.J. Zong, J.J. Wan, Y.Z. Qiao, et al. Cavitation endothelium damage of large artery vessel: a potential application to animal model of atherosclerosis[C]//The International Conference on Health Informatics. Springer, Cham, 2014: 63-66.10.1007/978-3-319-03005-0_17.

[31] A. Shi, P. Huang, S. Guo, et al., Precise spatial control of cavitation erosion in a vessel phantom by using an ultrasonic standing wave[J], Ultrason. Sonochem. 31 (2016) 163–172, https://doi.org/10.1016/j.ultsonch.2015.12.016.

[32] G. Silvani, C. Scognamiglio, D. Caprini, et al., Reversible cavitation-induced junctional opening in an artificial endothelial layer[J], Small 15 (51) (2019) 1905375, https://doi.org/10.1002/smll.201905375.

[33] P.T. Yemane, A.K.O. Åslund, S. Snipstad, et al., Effect of ultrasound on the vasculature and extravasation of nanoscale particles imaged in real time[J], Ultrasound Med. Biol. 45 (11) (2019) 3028–3041, https://doi.org/10.1016/j.ultrasmedbio.2019.07.683.

[34] E. Sassaroli, K. Hynynen, Resonance frequency of microbubbles in small blood vessels: a numerical study[J], Phys. Med. Biol. 50 (22) (2005) 5293, https://doi.org/10.1088/0031-9155/50/22/006.

[35] S. Qin, K.W. Ferrara, The natural frequency of nonlinear oscillation of ultrasound contrast agents in microvessels[J], Ultrasound Med. Biol. 33 (7) (2007) 1140–1148, https://doi.org/10.1016/j.ultrasmedbio.2006.12.009.

[36] H. Miao, S.M. Gracewski, D. Dalecki, Ultrasonic excitation of a bubble inside a deformable tube: implications for ultrasonically induced hemorrhage[J], J. Acoust. Soc. Am. 124 (4) (2008) 2374–2384, https://doi.org/10.1121/1.2967488.

[37] S. Martynov, E. Stride, N. Saffari, The natural frequencies of microbubble oscillation in elastic vessels[J], J. Acoust. Soc. Am. 126 (6) (2009) 2963–2972, https://doi.org/10.1121/1.3243292.

[38] W. Wiedemair, Ž. Tuković, H. Jasak, et al., On ultrasound-induced microbubble oscillation in a capillary blood vessel and its implications for the blood–brain barrier[J], Phys. Med. Biol. 57 (4) (2012) 1019, https://doi.org/10.1088/0031-9155/57/4/1019.

[39] C.Y. Chen, Y.Y. Gu, J. Du, et al., Microbubble oscillating in a microvessel filled with viscous fluid: a finite element modeling study[J], Ultrasonics 66 (2016) 54–64, https://doi.org/10.1016/j.ultras.2015.11.010.

[40] R. Singh, X. Wang, X. Yang, Cavitation induced shear and circumferential stresses on blood vessel walls during photo-mediated ultrasound therapy[J], AIP Adv. 10 (12) (2020), 125227, https://doi.org/10.1063/5.0020410.

[41] R. Singh, X. Yang, A 3D finite element model to study the cavitation induced stresses on blood–vessel wall during the ultrasound-only phase of photo-mediated ultrasound therapy[J], AIP Adv. 12 (4) (2022), 045020, https://doi.org/10.1063/5.0082429.

[42] G. Rigatelli, M. Zuin, C. Bilato, et al., Coronary artery cavitation as a trigger for atherosclerotic plaque progression: a simplified numerical and computational fluid dynamic demonstration[J], Rev. Cardiovasc. Med. 23 (2) (2022) 58, https://doi.org/10.31083/j.rcm2302058.

[43] C. Born, Z. Zhang, et al., Estimation of disruption of animal cells by laminar shear stress, Biotechnol. Bioeng. 40 (9) (1992) 1004–1010, https://doi.org/10.1002/bit.260400903.

[44] T.G. Leighton, The Acoustic Bubble, Academic Press, London, 1994, pp. 234–243, https://doi.org/10.1017/S0022112094214519.

[45] R. Zakerzadeh, P. Zunino, A computational framework for fluid–porous structure interaction with large structural deformation, Meccanica 54 (1–2) (2019) 101–121, https://doi.org/10.1103/PhysRevE.99.023109.

[46] E. Décavé, D. Garrivier, Y. Bréchet, et al., Shear flow-induced detachment kinetics of Dictyostelium discoideum cells from solid substrate[J], Biophys. J. 82 (5) (2002) 2383–2395, https://doi.org/10.1016/S0006-3495(02)75583-5.

[47] L. Junge, C.D. Ohl, B. Wolfrum, et al., Cell detachment method using shock-wave–induced cavitation[J], Ultrasound Med. Biol. 29 (12) (2003) 1769–1776, https://doi.org/10.1016/j.ultrasmedbio.2003.08.010.

[48] E. Décavé, D. Garrivier, Y. Bréchet, et al., Peeling process in living cell movement under shear flow[J], Phys. Rev. Lett. 89 (10) (2002), 108101, https://doi.org/10.1103/PhysRevLett.89.108101.

[49] L.A. Pérez-Maqueda, J.M. Criado, The accuracy of Senum and Yang's approximations to the Arrhenius integral [J], J. Therm. Anal. Calorim. 60 (3) (2000) 909–915, https://doi.org/10.1023/A:1010115926340.

[50] S. Qin, K.W. Ferrara, Acoustic response of compliable microvessels containing ultrasound contrast agents, Phys. Med. Biol. 51 (20) (2006) 5065–5088, https://doi.org/10.1088/0031-9155/51/20/001.

[51] A.R. Williams, Shear-induced fragmentation of human erythrocytes[J], Biorheology 10 (3) (1973) 303–311, https://doi.org/10.3233/BIR-1973-10303.

[52] Z. Zhang, M.A. Ferenczi, A.C. Lush, et al., A novel micromanipulation technique for measuring the bursting strength of single mammalian cells[J], Appl. Microbiol. Biotechnol. 36 (2) (1991) 208–210, https://doi.org/10.1007/BF00164421.

[53] W. Liu, J. Hu, Y. Liu, et al., Numerical analysis of the biomechanical effects on micro-vessels by ultrasound-driven cavitation[J], Acta Bioeng. Biomech. 23 (1) (2021), https://doi.org/10.37190/abb-01749-2020-03.

[54] M.H. Kural, G. Dai, L.E. Niklason, et al., An ex vivo vessel injury model to study remodeling[J], Cell Transp. 27 (9) (2018) 1375–1389.

[55] P. Zhong, Y. Zhou, S. Zhu, Dynamics of bubble oscillation in constrained media and mechanisms of vessel rupture in SWL[J], Ultrasound Med. Biol. 27 (1) (2001) 119–134, https://doi.org/10.1016/S0301-5629(00)00322-7.

[56] K.S. Furukawa, T. Ushida, T. Nagase, et al., Quantitative analysis of cell detachment by shear stress[J], Mater. Sci. Eng., C 17 (1–2) (2001) 55–58, https://doi.org/10.1016/S0928-4931(01)00336-8.

[57] I. Tzanakis, G.S.B. Lebon, D.G. Eskin, et al., Characterisation of the ultrasonic acoustic spectrum and pressure field in aluminium melt with an advanced cavitometer[J], J. Mater. Process. Technol. 229 (2016) 582–586, https://doi.org/10.1016/j.jmatprotec.2015.10.009.

[58] W. Lei, J. Hu, Y. Liu, et al., Numerical evaluation of high-intensity focused ultrasound-induced thermal lesions in atherosclerotic plaques[J], Math. Biosci. Eng 18 (2021) 1154–1168, https://doi.org/10.3934/mbe.2021062.

[59] E. Zilonova, M. Solovchuk, T.W.H. Sheu, Dynamics of bubble-bubble interactions experiencing viscoelastic drag[J], Phys. Rev. E 99 (2) (2019), 023109, https://doi.org/10.1103/PhysRevE.99.023109.

[60] O. Chaudhuri, J. Cooper-White, P.A. Janmey, et al., Effects of extracellular matrix viscoelasticity on cellular behaviour[J], Nature 584 (7822) (2020) 535–546, https://doi.org/10.1038/s41586-020-2612-2.

[61] P. Gupta, A. Srivastava, Non-Fourier transient thermal analysis of biological tissue phantoms subjected to high intensity focused ultrasound[J], Int. J. Heat Mass Transf. 136 (2019) 1052–1063, https://doi.org/10.1016/j.ijheatmasstransfer.2019.03.014.

[62] Y. Lu, B. Li, F. Xiong, et al., Simple discrete models for dynamic structure-soil-structure interaction analysis[J], Eng. Struct. 206 (2020), 110188, https://doi.org/10.1016/j.engstruct.2020.110188.

[63] K. Linka, M. Hillgärtner, M. Itskov, Fatigue of soft fibrous tissues: multi-scale mechanics and constitutive modeling[J], Acta Biomater. 71 (2018) 398–410, https://doi.org/10.1016/j.actbio.2018.03.010.